ORIGINAL ARTICLE

lajss.org© Latin American Journal of Solids and Structures

www.lajss.org

Shape Optimization of a Tram Front End for Passive Safety in Tram–Pedestrian Collisions

Jonghwan Park[a], Minseong Cho[b], Jaesun Lee[c]*, Hong-Lae Jang[d]*

[a] Department of Smart Manufacturing Engineering, Changwon National University, Changwon 51140, Republic of Korea. Email: 20257560@gs.cwnu.ac.kr

[b] Defense Manufacturing Engineering Team, Hyundai Rotem, Changwon 51407, Republic of Korea. Email: minseong@hyundai-rotem.co.kr

[c] School of Mechanical Engineering, Changwon National University, Changwon 51140, Republic of Korea. Email: jaesun@changwon.ac.kr

[d] Department of Railroad Operation Systems Engineering, Korea National University of Transportation, Uiwang 16106, Republic of Korea. Email: hjang@ut.ac.kr

* Corresponding authors

https://doi.org/10.1590/1679-7825/e9211

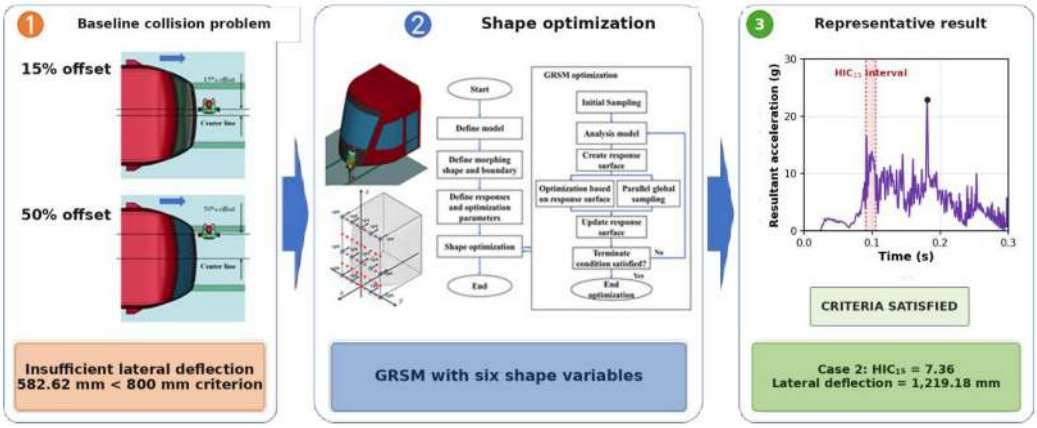
Abstract

This study presents a standards-oriented shape-optimization framework for modifying the front-end geometry of an existing tram. A finite element model was developed for the CEN/TR 17420 Type A scenario at 20 km/h using Hybrid III and VIVA+ AM50 pedestrian models. Although the baseline geometry satisfied the HIC15 requirement, lateral deflection at the 50% offset was only 582.62 mm for Hybrid III and 321.58 mm for VIVA+. Six front-end shape variables were parameterized by mesh morphing and optimized using the Global Response Surface Method (GRSM), with lateral deflection maximized subject to HIC15 and design-variable constraints. One selected design from each of the six optimization cases satisfied both Type A collision-response criteria. Across these designs, lateral deflection ranged from 895.25 to 1,284.46 mm, while HIC15 ranged from 7.36 to 711.49. The results show that mesh morphing and GRSM can support retrofit-oriented tram-front design by quantifying the trade-off among lateral deflection, HIC15, and the allowable extent of front-end modification.

Keywords

tram–pedestrian collision, CEN/TR 17420, passive safety, finite element analysis, mesh morphing, surrogate-based optimization

Graphical Abstract



Received July 23, 2026. In revised form August 14, 2026. Accepted August 16, 2026. Available online August 19, 2026.
https://doi.org/10.1590/1679-7825/e9211

Latin American Journal of Solids and Structures. ISSN 1679-7825. Copyright © 2026. This is an Open Access article distributed under the terms of the Creative Commons Attribution License, which permits unrestricted use, distribution, and reproduction in any medium, provided the original work is properly cited.

1 INTRODUCTION

The renewed use of trams and light rail vehicles is closely linked to the demand for high-capacity and low-emission urban transport. Unlike grade-separated rail systems, however, a substantial part of a tram network is embedded in public streets, at intersections, or near boarding platforms. Trams therefore interact continuously with pedestrians, cyclists, and road vehicles in a constrained right-of-way. Although tram transport is generally safe for passengers, collisions with unprotected road users can have severe consequences because of the large vehicle mass, long braking distance, and limited ability to perform an evasive maneuver. Infrastructure and operational measures can reduce crash occurrence, but vehicle-based passive safety remains necessary because conflicts cannot be eliminated completely.

Accident studies provide a consistent justification for considering pedestrian protection in tram design. An analysis of 7,535 tram–pedestrian crashes and 8,802 pedestrian injuries in several European countries reported that pedestrians form the largest group of fatal tram-crash casualties and that head injuries are prominent across injury severities (Lackner et al. 2022). In the same database, 3% of reported pedestrian injuries were fatal and 23% were severe. Studies of Melbourne tram routes identified travel speed, traffic volume, lane priority, tram age, and floor height as significant factors in serious injury crashes (Naznin et al. 2016). Gaca and Franek (2021), using more than 400 tram–pedestrian cases, further demonstrated the strong nonlinear relationship between impact speed and fatality risk. These findings indicate that accident prevention and passive injury mitigation must be developed as complementary layers of safety.

The kinematics of a struck pedestrian are governed by more than the initial contact force. The height and protrusion of the lower front determine engagement of the legs and pelvis, while the front slope and windshield inclination affect torso rotation, head-contact location, and subsequent trajectory. Ground clearance is also important because it influences the possibility of underrun. Early simulation work showed that practical changes to tram geometry can reduce injury risk and identified the windshield, front cover, A-pillars, and lower edge as critical regions (Weber et al. 2015). Chevalier et al. (2019) systematically explored 8,840 tram-shape and pedestrian-size combinations and identified two competing mechanisms: lower-body engagement can rotate the torso and increase head impact velocity, whereas shoulder loading can accelerate the upper body away from the windshield. Thus, a geometry that improves one response measure does not necessarily improve every aspect of pedestrian kinematics.

Experimental and numerical studies published after the introduction of dedicated tram-safety guidance have expanded this understanding. Full-scale and component-level tests have quantified the effects of impact speed, pedestrian orientation, and laminated windshield response on head loading (Lopot et al. 2023; Jezdik et al. 2023). Secondary impact with the ground can also govern head injury even when primary tram contact is not critical (Tomsovsky et al. 2022). Numerical tram-impact studies have likewise shown the importance of explicitly resolving pedestrian contact and body motion throughout the primary phase (Spirk et al. 2022). Peng et al. (2024) evaluated both head and lower-limb responses and confirmed that impact configuration and vehicle-front characteristics affect different body regions in different ways. Collectively, these studies support the use of a kinematics-based assessment rather than a single local injury measure.

CEN/TR 17420 provides the first dedicated design framework for the passive safety of trams and light rail vehicles. It defines a preferred geometric route and, for fronts that do not satisfy the recommended geometry, a Type A numerical collision scenario at 20 km/h. The scenario evaluates HIC15 together with the lateral deflection of the pedestrian. Recent applications have used the standard to assess improved generic tram fronts with detailed human body models (Lackner et al. 2023) and a novel very-light-rail vehicle with an anthropomorphic test device (Bethell et al. 2024). These studies demonstrate the feasibility of virtual testing, but they primarily compare predefined front concepts rather than seeking an optimal modification of an existing geometry.

The choice of pedestrian model is another source of uncertainty. ATDs offer repeatability and established injury measures, whereas finite element human body models represent anatomical geometry, distributed contact, and local deformation in greater detail. The VIVA+ model family was developed to support sex- and size-sensitive virtual safety assessment and has been evaluated under a range of blunt-impact conditions (John et al. 2022). Reviews of pedestrian simulation emphasize that multibody, ATD, and detailed finite element models have different strengths and validation domains (Wdowicz and Ptak 2023). For tram impacts, Lackner et al. (2023) showed that HBM-based assessment can reveal body-region responses and kinematic changes that are not captured by a single global injury criterion. It is therefore useful to verify the design diagnosis with more than one model type.

Optimization under impact loading is computationally intensive because every design evaluation requires a nonlinear transient analysis and because contact changes can produce a non-smooth response. Response-surface and surrogate-based methods are widely used to reduce this cost by approximating the relation between design variables and crash responses (Forsberg and Nilsson 2006; Wang and Shan 2007; Forrester et al. 2008). In railway applications, related crashworthiness studies have concentrated on energy-absorbing components and their geometric optimization (Kim and Jung 2021; Ji et al. 2021; Ahn et al. 2021), rather than direct optimization of lateral deflection. Within LAJSS, finite element analysis has been coupled with

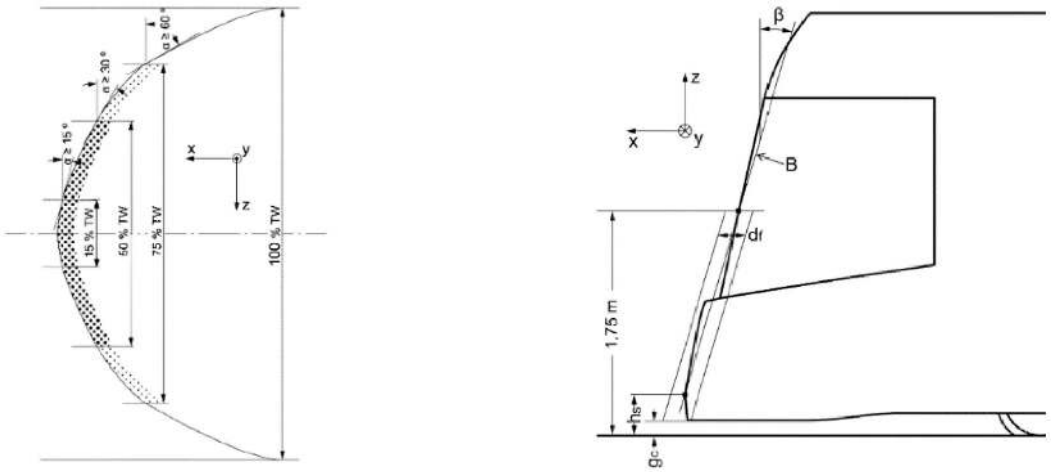
Taguchi sensitivity analysis for occupant head protection (Asadinia et al. 2018), and response surfaces have been combined with evolutionary optimization for thin-walled energy absorbers (Usta et al. 2018). More recently, multi-objective surrogate optimization has been applied to side-impact crashworthiness of battery enclosures (Yay et al. 2025). These studies establish the suitability of surrogate-assisted design for impact problems, but their objectives concern structural energy absorption or restrained occupants rather than the coupled HIC15 and lateral-deflection requirements for an unrestrained pedestrian.

Accordingly, a clear research gap remains between standards-based tram assessment and numerical shape optimization. Published tram studies have generally evaluated a limited number of predefined front shapes, whereas crashworthiness-optimization studies have primarily addressed structural energy absorbers or occupant-restraint parameters. The present study bridges these areas through a retrofit-oriented workflow integrating (i) CEN/TR 17420 geometric screening, (ii) baseline finite element collision assessment using both an ATD and an HBM, (iii) six-variable mesh-morphing parameterization of an existing tram front, and (iv) adaptive GRSM optimization under case-specific HIC15 limits and common design-variable upper bounds. Within this framework, the tram-front geometry constitutes the design input, changes in the pedestrian contact sequence and body motion provide the physical response mechanism, lateral deflection is maximized as the objective, HIC15 is imposed as the response constraint, and the six morphing variables are bounded by common side constraints. The study therefore does not seek an isolated geometric improvement or propose a universal tram-front shape. Instead, it quantifies how the HIC15 limit and the common design-variable upper bound affect the attainable lateral deflection and provides a parametric basis for subsequent selection of front-end modifications in view of project-specific design margins and manufacturing constraints.

2 PASSIVE-SAFETY CRITERIA AND COLLISION SCENARIO

2.1 CEN/TR 17420 geometric assessment

CEN/TR 17420 divides a tram–pedestrian collision into successive phases and identifies the initial vehicle–pedestrian interaction as the phase most directly controlled by the tram front. The impact surface extends across 75% of the vehicle width and from the lower front to a height of 1.75 m. The geometric quantities used for preliminary assessment are shown in Figure 1 and summarized in Table 1. A design that fails this geometric assessment can be evaluated using the prescribed Type A collision scenario.



(a) Definition of α (b) Definitions of h_s, Line B, β, d_f, and g_c

Figure 1 Definition of the impact surface and geometric parameters.

Table 1 Geometric parameters and CEN/TR 17420 criteria.

Parameter	Description	Criterion
h_s	Height of the maximum front protrusion	$h_s \leq 350$ mm
α	Projected impact-surface tangent angle	$\alpha_{15} \geq 15°$; $\alpha_{50} \geq 30°$; $\alpha_{75} \geq 60°$
Line B	Line from maximum protrusion to top of impact surface	—
β	Slope of Line B	$\beta \geq 10°$
d_f	Offset region relative to Line B	$d_f \leq 250$ mm
g_c	Ground clearance	$g_c \leq 250$ mm

2.2 Type A collision scenario and response measures

The Type A collision scenario was configured in accordance with CEN/TR 17420. It represents a standing pedestrian struck by a tram traveling at a prescribed constant velocity of 20 km/h. Simulations were conducted at lateral positions corresponding to 15% and 50% of the tram width, as illustrated in Figure 2. The tram–pedestrian friction coefficient was set to zero in accordance with the idealized contact condition specified for the Type A assessment.

Passive-safety performance was evaluated using HIC15 and lateral deflection, as specified for the Type A collision assessment. HIC15 was calculated from the resultant head acceleration over the most critical time interval not exceeding 15 ms:

$$\mathrm{HIC}_{15} = \max_{0<t_2-t_1\le 0.015}\left[(t_2-t_1)\left(\frac{1}{t_2-t_1}\int_{t_1}^{t_2} a(t)\mathrm{d}t\right)^{2.5}\right] \tag{1}$$

where $a(t)$ is the resultant acceleration of the head expressed in units of gravitational acceleration g, and t_1 and t_2 are expressed in seconds. HIC15 was used instead of HIC36 because the Type A procedure of CEN/TR 17420 specified a 15-ms evaluation interval for the tram-pedestrian impact assessment. The acceptance limits were $\mathrm{HIC}_{15} \le 1{,}000$ and $D \ge 800$ mm, where *D* denotes the pedestrian lateral deflection. Accordingly, the tram-front shape was treated as the design input, lateral deflection D as the kinematic objective to be maximized, and HIC15 as the injury-related response constraint. The complete optimization formulation and the case-specific constraint values are presented in Section 4.2.



Figure 2 Pedestrian positions in the Type A collision scenario.

2.3 Pedestrian representations

Two numerical pedestrian representations were considered to reduce the dependence of the baseline assessment on a single model type, as shown in Figure 3. The LSTC Hybrid III 50th-percentile male model was employed as the anthropomorphic test device (ATD) following the Type A collision assessment procedure described in CEN/TR 17420. The Hybrid III 50th-percentile male dummy has also been used in previous tram–pedestrian impact research (Tomsovsky et al. 2022), supporting its use as a repeatable reference model for the present assessment.

The VIVA+ AM50 model was additionally employed as an anatomically detailed finite element human body model (HBM). The ATD provides a repeatable reference for evaluating global kinematics and established injury measures, whereas the HBM represents anatomical geometry, body-segment compliance, and distributed contact in greater detail. Previous comparative studies have shown that predicted kinematics and injury measures can vary with the selected ATD or HBM formulation (Decker et al. 2019; Devane et al. 2023). The paired assessment was therefore intended to determine whether the two model types provided a consistent safety diagnosis of the baseline tram, rather than to demonstrate agreement in their numerical responses or to represent complete population variability.

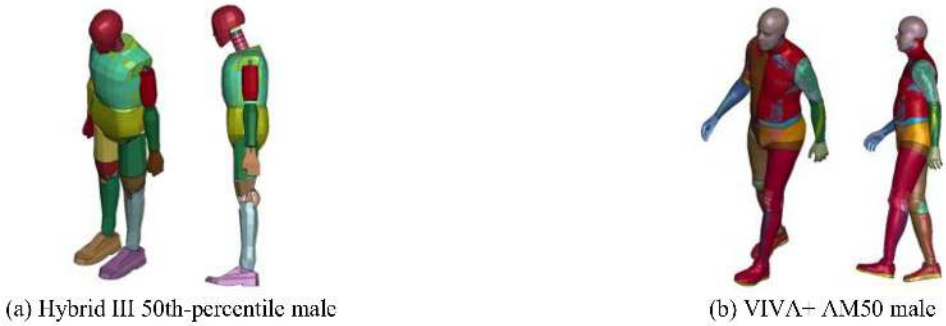


Figure 3 Finite element pedestrian models used in the collision assessment.

3 FINITE ELEMENT COLLISION MODEL

3.1 Tram model and geometric screening

The finite element model included the tram front-end region directly involved in the initial interaction with the pedestrian, as shown in Figure 4. The geometric assessment results for the baseline tram are summarized in Table 2. The principal tram components comprised the steel structural front, glass windshield, and plastic lamp cover. The material properties are summarized in Table 3, while the corresponding post-yield relationships are presented in Figure 5. To isolate the effects of front-end geometry in the comparative shape-optimization study, the Hybrid III pedestrian model, material definitions, contact settings, boundary conditions, impact velocity, and solver controls were kept unchanged across the baseline and all morphed designs evaluated in the optimization.

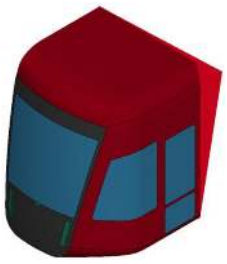


Figure 4 Finite element model of the tram front end.

Table 2 Geometric assessment of the baseline tram.

Parameter	Position	Value	Result
h_s	—	396 mm	Fail
α	15%	3.88°	Fail
α	50%	12.93°	Fail
α	75%	52.71°	Fail
β	—	7.92°	Fail
d_f	—	Not satisfied	Fail
g_c	—	190 mm	Pass

The steel, glass, and plastic components of the tram front were modeled using the LS-DYNA *MAT_PIECEWISE_LINEAR_PLASTICITY material model. The elastic response was defined by the Young's modulus and Poisson's ratio listed in Table 3, while the onset of plastic deformation was determined by the corresponding yield stress. The post-yield behavior was defined using piecewise-linear relationships between effective plastic strain and true effective stress, as shown in Figure 5. At zero effective plastic strain, the stress corresponds to the initial yield stress, and the subsequent data points define the material hardening behavior with increasing plastic strain.

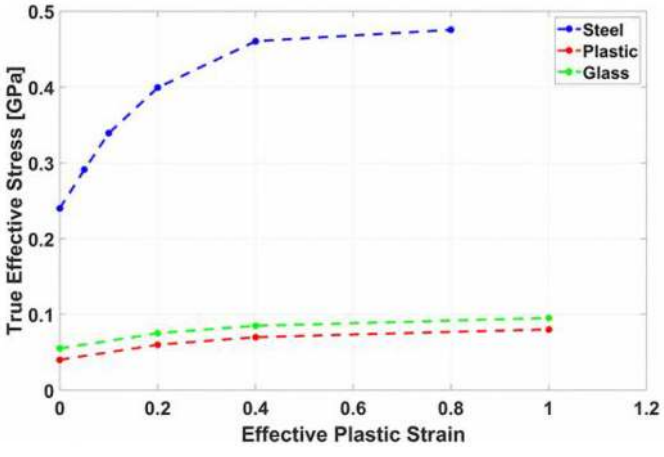


Figure 5 Post-yield material curves used in the piecewise-linear plasticity model.

Table 3 Material properties used for the tram model.

Material	Density (kg/m^3)	Young's modulus (GPa)	Poisson's ratio	Yield stress (MPa)
Steel	7,800	210	0.30	240
Glass	1,700	17	0.22	50
Plastic	1,200	2.8	0.30	40

3.2 Numerical implementation

The collision problem was solved as a nonlinear explicit transient analysis in LS-DYNA. The tram was assigned the prescribed impact velocity, whereas the pedestrian was initially positioned in the standing configuration defined for the Type A scenario. The simulation duration was selected to include the primary vehicle–pedestrian interaction and the time window required to determine the maximum HIC15 and lateral deflection. Contact was enforced throughout the event, and the same contact, boundary, output, and termination definitions were used for the baseline and all morphed designs. The zero tangential friction specified by CEN/TR 17420 was applied at the tram–pedestrian interface; the internal definitions and joint properties supplied with the Hybrid III and VIVA+ model releases were retained without modification.

A consistent numerical procedure was maintained throughout the comparative study. Model connectivity, initial contact, element quality, solution stability, energy histories, and pedestrian kinematics were checked during preprocessing and post-processing. Applying the same solver controls and model definitions to every design limited numerical inconsistency between the baseline and all morphed designs and allowed the observed response changes to be attributed primarily to the prescribed front-end geometry.

The material descriptions in Table 3 were kept deliberately consistent across the design cases because the study compares the kinematic effect of front shape rather than proposing a material or structural crashworthiness redesign. This assumption avoids confounding geometric effects with case-dependent stiffness or failure parameters, but it also means that the computed head response should be interpreted as a comparative design indicator. In particular, fracture, delamination, and detailed rate-dependent behavior of the laminated windshield were not resolved; experimental studies show that these mechanisms can influence head loading during tram impact (Jezdik et al. 2023).

3.3 Baseline collision response

The baseline simulations were performed in LS-DYNA using the setup shown in Figure 6. Both pedestrian models produced HIC15 values well below 1,000. The Hybrid III head did not make the same direct windshield contact observed for VIVA+ AM50, which explains the different acceleration histories in Figure 7. This difference illustrates why a low HIC15 value alone should not be interpreted as evidence of favorable whole-body kinematics. The baseline collision responses for both pedestrian models are summarized in Table 4.

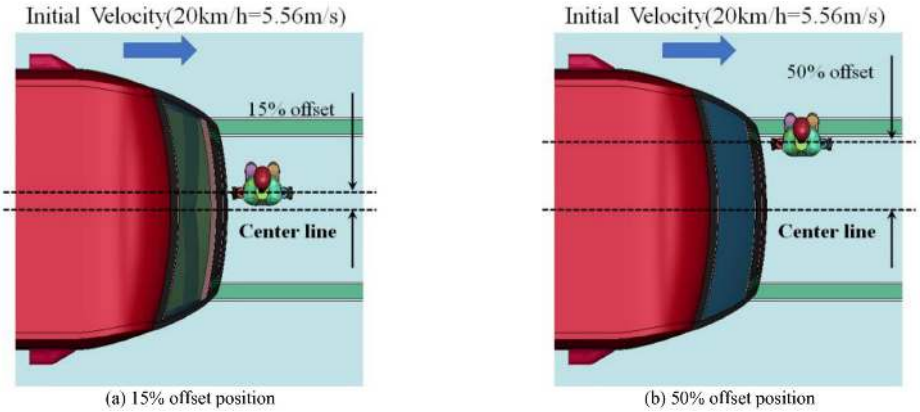


Figure 6 Finite element setup for tram–pedestrian collision analysis.

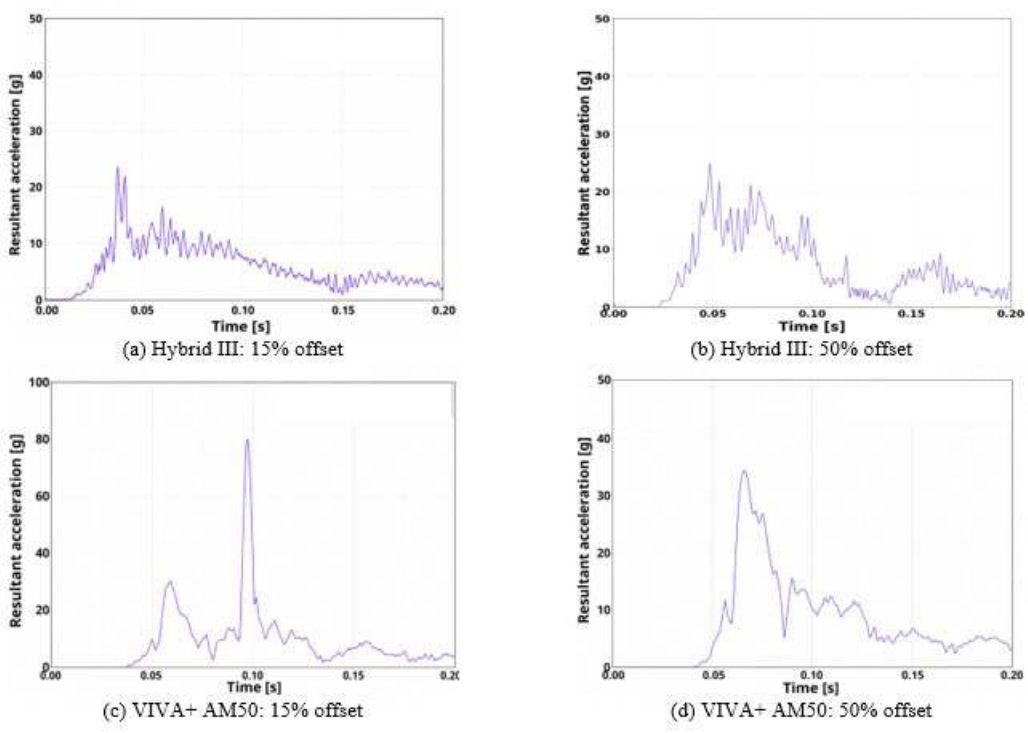


Figure 7 Resultant head-acceleration histories for the baseline collision cases.

Table 4 Collision responses of the baseline tram.

Pedestrian model	Offset	HIC15	Lateral deflection (mm)
Hybrid III (ATD)	15%	18.8	—
Hybrid III (ATD)	50%	21.6	582.62
VIVA+ AM50 (HBM)	15%	203.9	—
VIVA+ AM50 (HBM)	50%	83.2	321.58

At the 50% offset, the lateral deflections were 582.62 mm for Hybrid III and 321.58 mm for VIVA+ AM50, both below the required 800 mm. The baseline model therefore satisfied the HIC15 criterion but did not achieve the required lateral deflection. This result motivated the maximization of lateral deflection, with HIC15 retained as the response constraint.

4 SHAPE PARAMETERIZATION AND OPTIMIZATION

The optimization framework combines direct mesh morphing with the Global Response Surface Method (GRSM). Figure 8 illustrates the generic morphing concept, in which an initial mesh is transformed within prescribed upper and lower bounds and intermediate shapes are generated by moving the control points. Figure 9 summarizes the complete GRSM workflow from model definition and initial sampling to response-surface updating and termination.

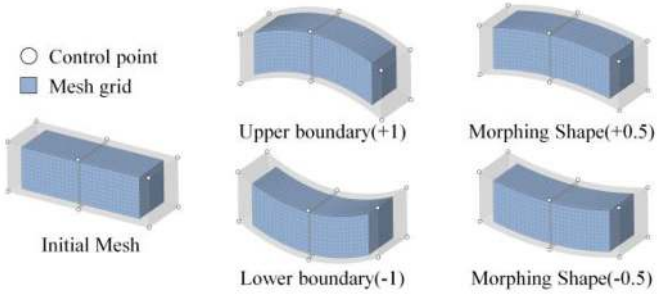


Figure 8 Description of parameterization using morphing.

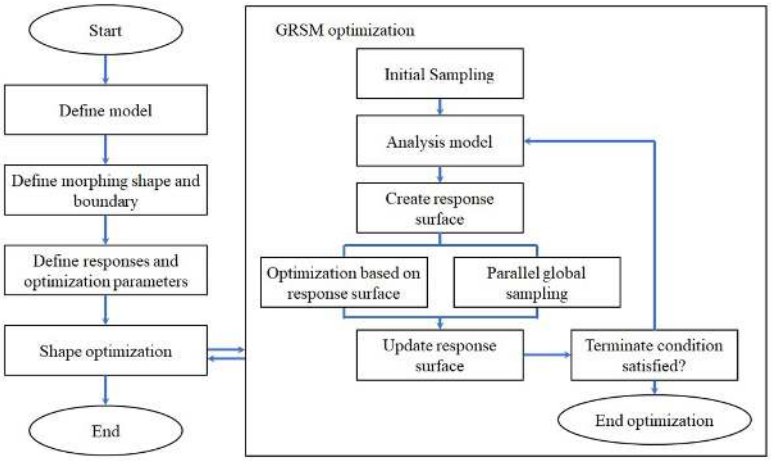


Figure 9 Flow chart for the GRSM optimization method.

4.1 Mesh-morphing parameterization

Mesh morphing was used to modify the existing finite element geometry without rebuilding the model for every design. A set of control points defined the deformation field, and six design variables, $x_i \left(i = 1, \cdots, 6\right)$, governed the front-end curvature in the horizontal and vertical planes (Figures 10 and 11). Each x_i, expressed in millimetres, represents the displacement amplitude of the corresponding morphing control-point group. The parameterization was selected to increase the α and β angles while preserving a smooth transition to the unchanged surrounding geometry. This approach is suited to retrofit studies because it operates directly on the analysis mesh and retains model connectivity.

Figure 8 illustrates the generic normalized morphing concept, in which the upper and lower boundary shapes define the allowable deformation envelope. For the tram optimization, each design variable varied from the baseline value $x_i = 0$ to the case-dependent upper bound *B*, as defined in Section 4.2. The control-point motion was transferred to the enclosed mesh through the morphing field, changing the front curvature without altering the original mesh topology. The control points were arranged around the impact surface, and each design variable was assigned to one of the principal horizontal or vertical curvature regions shown in Figures 10 and 11.

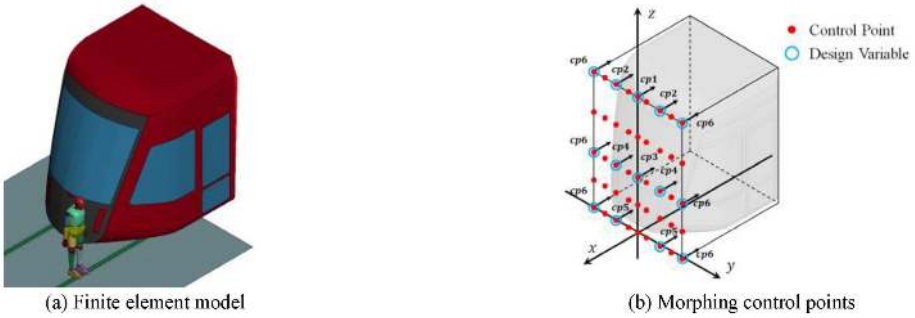


Figure 10 Mesh-morphing representation of the baseline tram front.

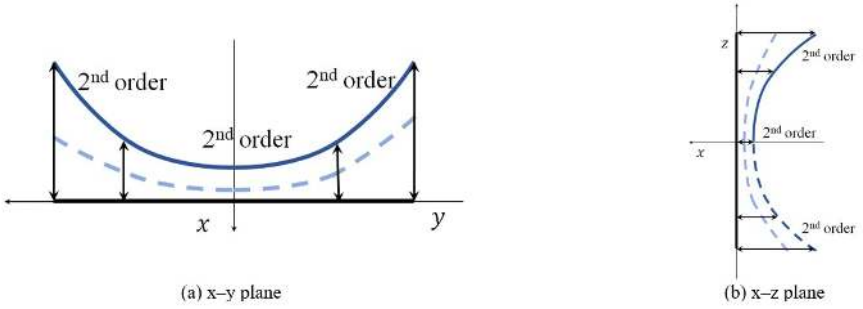


Figure 11 Six-variable shape parameterization in the horizontal and vertical planes.

After each morphing operation, the analysis deck was subjected to the same pre-run model checks as the baseline mesh. Particular attention was paid to element Jacobian, aspect ratio, warpage, skewness, shell-normal consistency, and unintended initial contact. Designs producing inverted or severely distorted elements were excluded before collision analysis so that the optimization did not gain an artificial advantage from a numerically unacceptable mesh.

4.2 Global Response Surface Method and optimization formulation

Direct optimization of crash simulations is computationally demanding because each design evaluation requires a nonlinear transient analysis and the collision response may vary nonlinearly with changes in contact geometry. The Global Response Surface Method (GRSM), as implemented in HyperStudy, was therefore employed as a response-surface-assisted global optimization method (Pajot 2013; Altair Engineering Inc. 2021). For each optimization case, HyperStudy generated an initial design of experiments (DOE) comprising eight designs, and the corresponding LS-DYNA responses were used to construct the initial response surface. In each of the subsequent 21 adaptive iterations, response-surface-based optimization and global sampling generated two candidate designs; both were evaluated using LS-DYNA, and their responses were returned to GRSM to update the response surface. Thus, each case comprised 50 high-fidelity evaluations, giving 300 evaluations across the six cases. Each run terminated when its prescribed 50-evaluation budget was reached.

As summarized in Figure 9, each adaptive iteration uses the newly obtained high-fidelity responses to update the response surface. The updated surface is then searched for improved feasible designs, while global sampling maintains exploration of less-sampled regions of the design space. Consequently, the sequence of individual LS-DYNA responses need not be monotonic. Optimization progress is instead represented by the objective history presented in Section 5.1. This behavior is particularly relevant to the present pedestrian-impact problem because small changes in front-end geometry can alter the contact sequence and produce nonlinear changes in HIC15 and lateral deflection.

The optimization objective was to maximize lateral deflection, while HIC15 was imposed as a response constraint and the six morphing design variables were bounded by common side constraints. Three HIC15 upper limits (A=1,000, 100, or 50) and two common design-variable upper bounds (B=1,000 or 500 mm) were combined to define the six optimization cases summarized in Table 5. These cases were used to quantify how the prescribed HIC15 limit and allowable geometric modification range affect the attainable lateral deflection.

The optimization problem for each case was formulated as follows:

$$\begin{aligned} &\underset{\mathbf{x}}{\text{maximize}} \quad D(\mathbf{x}) \\ &\text{subject to} \quad \mathrm{HIC}_{15}(\mathbf{x}) \le A, \\ &\qquad\qquad 0 \le x_i \le B \ (i = 1, \ldots, 6) \end{aligned} \tag{2}$$

Here, $\mathbf{x} = \left[x_1, \quad x_2, \quad \cdots, \quad x_6\right]^T$ denotes the vector of the six morphing design variables, and $D(\mathbf{x})$ represents the lateral deflection. The parameters A and B denote the case-specific HIC15 upper limit and the common upper bound of the six design variables, respectively. The CEN/TR 17420 requirement of D≥800 mm was used as an acceptance criterion for interpreting the evaluated designs, not as an additional constraint in Eq. (2), because D was the objective to be maximized.

Table 5 Complete optimization formulation for the six cases.

Case	Objective	Design variables	Response constraint	Side constraints
1	Maximize D(x)	$\mathbf{x} = [x_1, \ldots, x_6]^T$	$\mathrm{HIC}_{15}(\mathbf{x}) \le 1{,}000$	$0 \le x_i \le 1{,}000$ mm
2			$\mathrm{HIC}_{15}(\mathbf{x}) \le 100$	
3			$\mathrm{HIC}_{15}(\mathbf{x}) \le 50$	
4			$\mathrm{HIC}_{15}(\mathbf{x}) \le 1{,}000$	$0 \le x_i \le 500$ mm
5			$\mathrm{HIC}_{15}(\mathbf{x}) \le 100$	
6			$\mathrm{HIC}_{15}(\mathbf{x}) \le 50$	

Note: D(x) denotes lateral deflection. The 800-mm requirement was used as an acceptance criterion for interpreting the evaluated designs, not as an additional constraint in Eq. (2). For all cases, i = 1, …, 6.

The response surface guided candidate generation after the initial DOE, but all 50 evaluated designs in each case were analyzed using nonlinear LS-DYNA. Accordingly, the objective and constraint histories and the HIC15 and lateral-deflection values reported in Table 7 are based on high-fidelity analyses rather than surrogate predictions. For each case, the selected design was the feasible high-fidelity evaluation that produced the largest lateral deflection within the prescribed 50-evaluation budget.

Although CEN/TR 17420 specifies HIC15≤1,000 and D≥800 mm for the Type A assessment, practical tram development may also involve project-specific requirements, design margins, and manufacturing constraints on the modification of an existing front end. The stricter HIC15 limits and the two morphing bounds were therefore introduced as parametric design conditions to quantify the trade-off between lateral deflection, head response, and the allowable extent of geometric modification; they are not additional requirements of CEN/TR 17420.

5 OPTIMIZATION RESULTS

5.1 Objective and constraint histories and selected geometry

The GRSM objective and constraint histories are presented in Figures 12 and 13. Each gray dot or red cross represents a high-fidelity LS-DYNA evaluation generated during the initial DOE or the subsequent adaptive GRSM iterations. The blue step curve is the objective history and is updated only when a newly evaluated design satisfies the constraints in Eq. (2) and yields a larger lateral deflection than the previously selected design. The purple curve is the corresponding constraint-utilization history, expressed as HIC15/A, for the design defining the objective history.

Because GRSM combines response-surface-based optimization with global exploration, the individual high-fidelity evaluations and their HIC15 values need not vary monotonically. The stepwise increase in the objective history shows that improved feasible designs were identified as the response surface was updated, consistent with the characteristic GRSM objective history described by Pajot (2013). The green circle marks the first evaluated design satisfying HIC15 ≤ A and D ≥ 800 mm, whereas the black diamond marks the selected design with the largest feasible D within the prescribed 50-evaluation budget.

The objective histories also show that Cases 1–3, with B = 1,000 mm, attained larger lateral deflection than Cases 4–6, with B = 500 mm. This comparison demonstrates that the allowable morphing range strongly influenced the attainable lateral deflection.

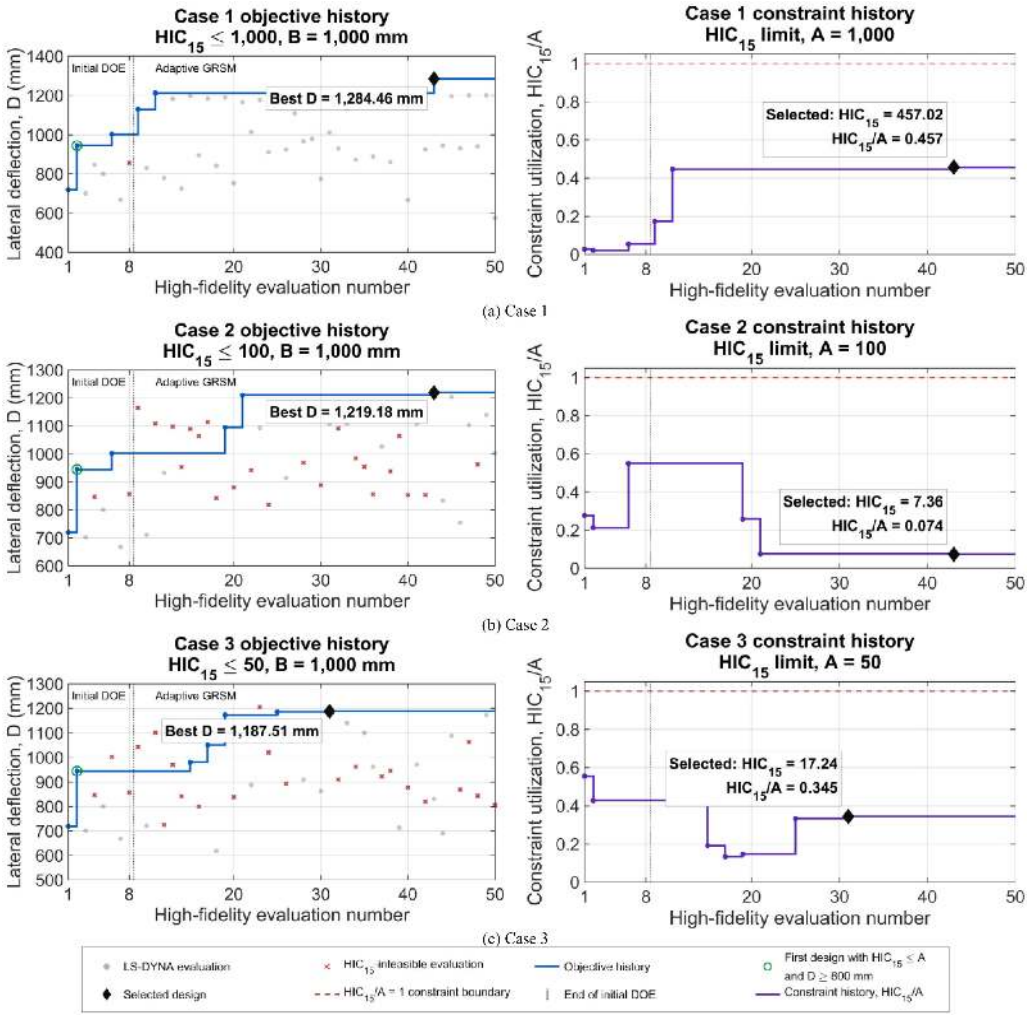


Figure 12 GRSM objective and constraint histories for Cases 1–3.

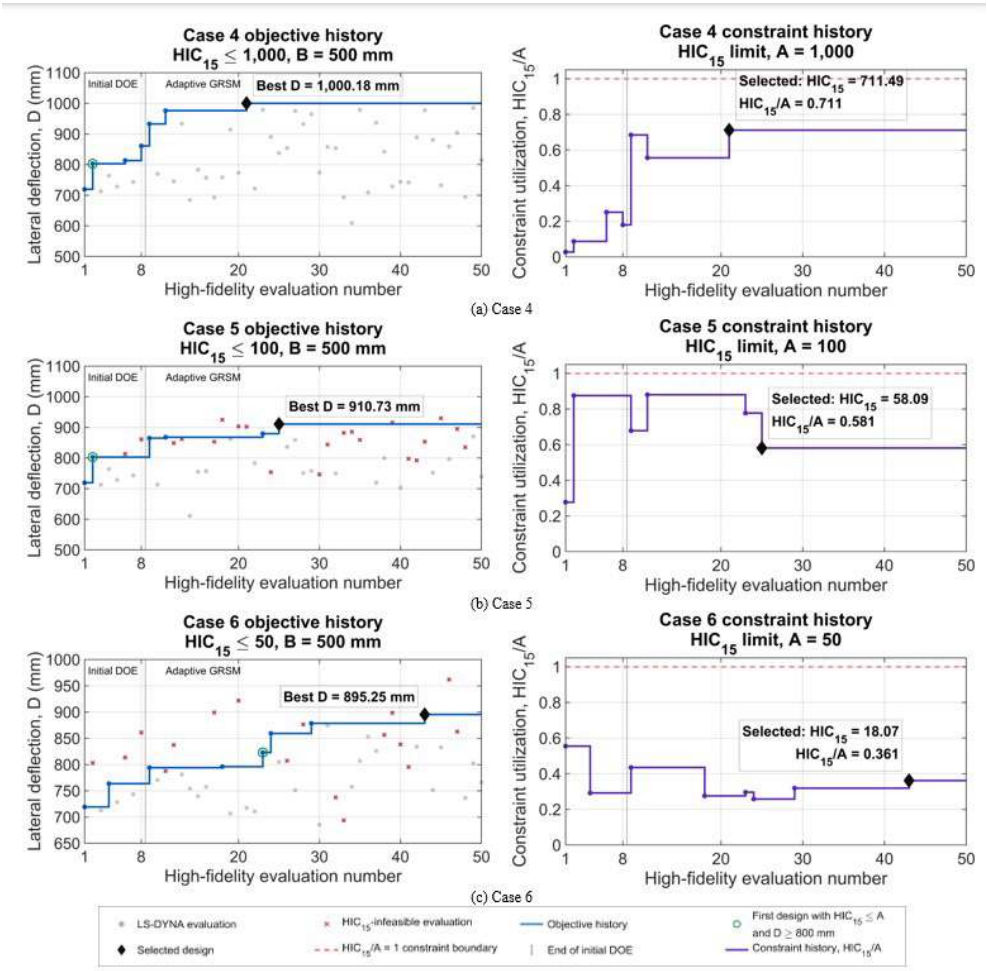


Figure 13 GRSM objective and constraint histories for Cases 4–6.

The selected front-end geometries for the six optimization cases are shown in Figure 14, and their horizontal and vertical profiles are compared with the baseline in Figure 15. The larger design-variable bound in Cases 1–3 allowed greater changes in the front profile than the 500-mm bound in Cases 4–6. The corresponding α and β values are listed in Table 6.

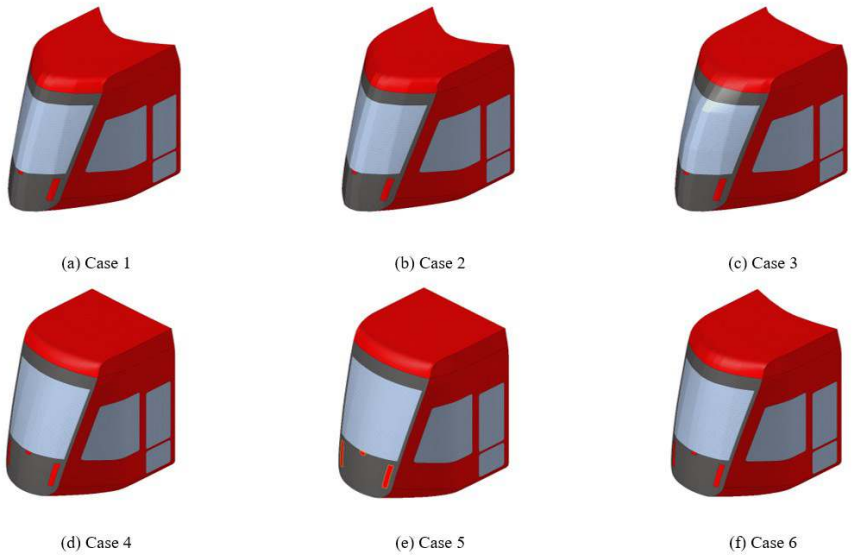


Figure 14 Selected tram-front geometries for the six optimization cases.

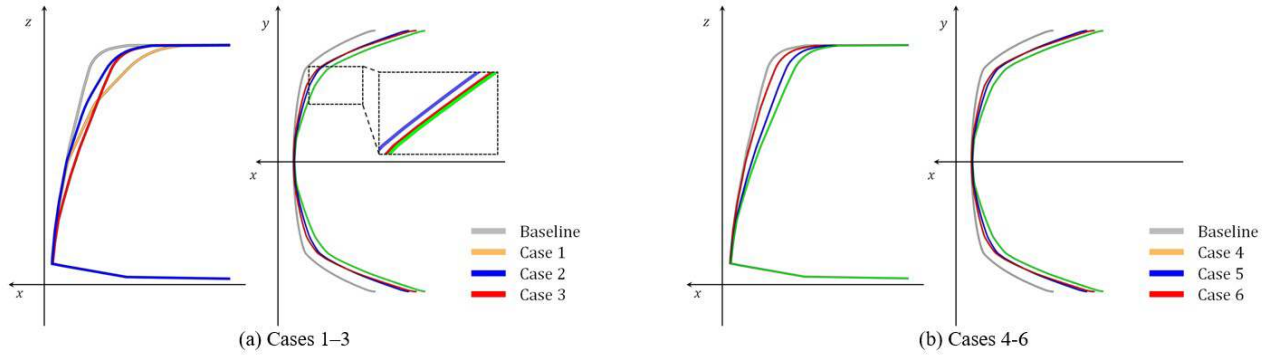


Figure 15 Comparison of the baseline and selected front-end profiles: (a) Cases 1–3; (b) Cases 4–6.

Table 6 Geometric parameters of the baseline and selected designs.

Model	Constraint limits	α_{15} (°)	α_{50} (°)	α_{75} (°)	β (°)
Baseline	—	3.88	12.93	52.71	7.92
Case 1	A = 1,000; B = 1,000 mm	29.96	51.20	72.00	11.67
Case 2	A = 100; B = 1,000 mm	29.26	50.25	71.85	8.34
Case 3	A = 50; B = 1,000 mm	30.21	51.13	72.44	8.91
Case 4	A = 1,000; B = 500 mm	12.55	32.74	69.67	12.95
Case 5	A = 100; B = 500 mm	8.95	26.52	67.60	11.64
Case 6	A = 50; B = 500 mm	7.29	28.53	69.73	8.76

Cases 1–3 satisfied all three α-angle criteria, but only Case 1 also satisfied β ≥ 10°. Under the tighter design-variable bound, Cases 4–6 satisfied the α75 criterion but failed the α15 criterion. Case 4 additionally satisfied α50 and β, Case 5 satisfied β only, and Case 6 satisfied neither α50 nor β. These results illustrate the alternative assessment route in CEN/TR 17420: a front that does not satisfy every geometric recommendation may nevertheless satisfy the Type A collision-response criteria, provided that HIC15 ≤ 1,000 and D ≥ 800 mm.

5.2 Collision responses of the selected designs

Table 7 Collision responses of the selected designs.

Model	Constraint limits	HIC15	Lateral deflection (mm)
Baseline	—	21.60	582.62
Case 1	A = 1,000; B = 1,000 mm	457.02	1,284.46
Case 2	A = 100; B = 1,000 mm	7.36	1,219.18
Case 3	A = 50; B = 1,000 mm	17.24	1,187.51
Case 4	A = 1,000; B = 500 mm	711.49	1,000.18
Case 5	A = 100; B = 500 mm	58.09	910.73
Case 6	A = 50; B = 500 mm	18.07	895.25

Figure 16 presents the resultant head-acceleration histories and HIC15 evaluation intervals for the six selected designs. All six selected designs satisfied the Type A collision-response criteria, with HIC15 below 1,000 and lateral deflection above 800 mm (Table 7). Case 1 produced the largest lateral deflection of 1,284.46 mm, whereas Case 6 produced the smallest value of 895.25 mm. The latter still exceeded the 800-mm criterion by 95.25 mm. Cases 1–3, with B = 1,000 mm, consistently achieved larger lateral deflection than Cases 4–6, with B = 500 mm, confirming that the design-variable bound strongly affected the attainable objective value.

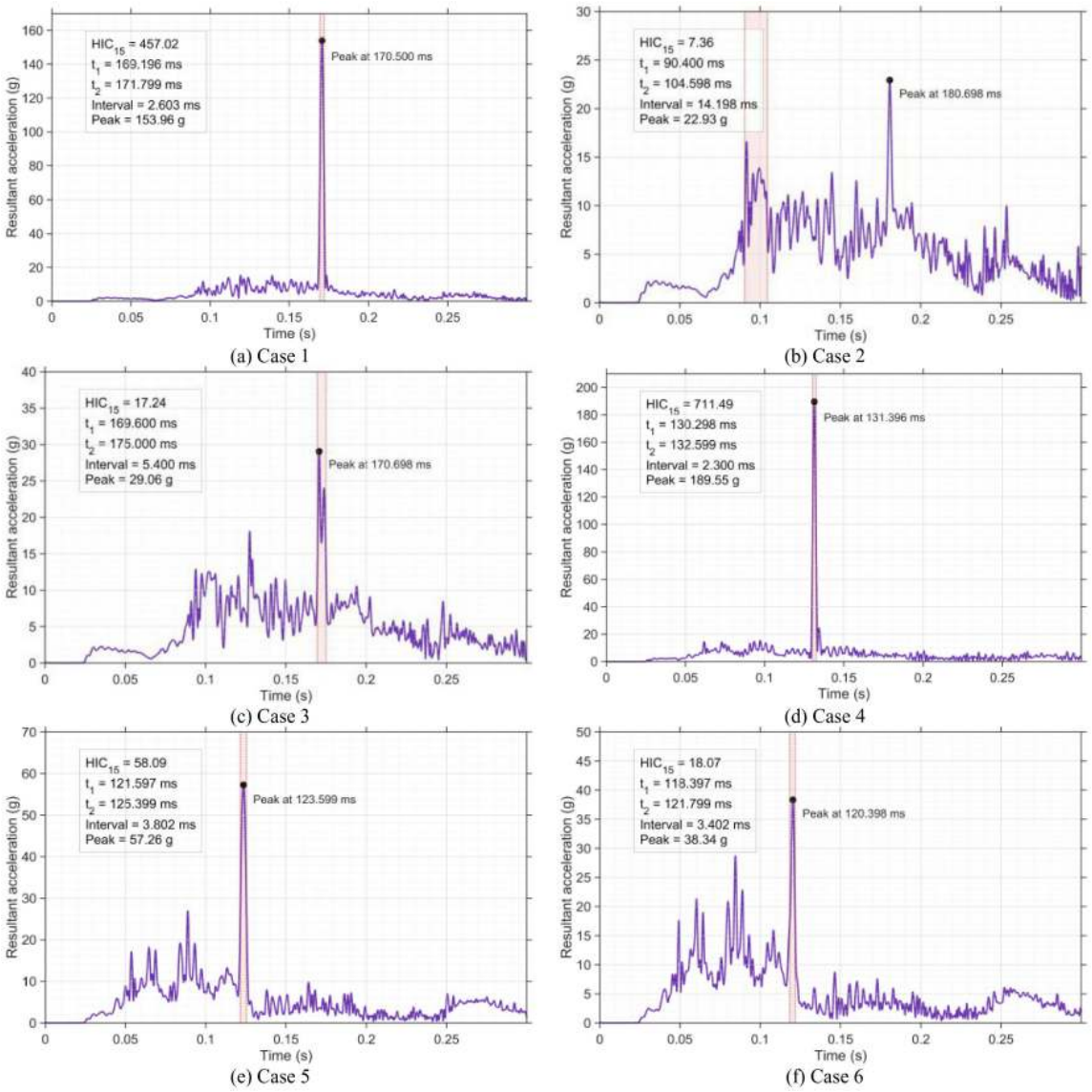


Figure 16 Resultant head-acceleration histories and HIC15 evaluation intervals for the selected designs.

Relative to the baseline Hybrid III result, lateral deflection increased by 103.8–120.5% in Cases 1–3 and by 53.7–71.7% in Cases 4–6. Tightening A from 1,000 to 100 reduced lateral deflection by 5.1% from Case 1 to Case 2 while reducing HIC15 by 98.4%. The corresponding comparison between Cases 4 and 5 showed an 8.9% reduction in lateral deflection and a 91.8% reduction in HIC15. These comparisons show that tightening the HIC15 limit can substantially reduce the head response with a relatively modest decrease in lateral deflection, whereas reducing B from 1,000 to 500 mm has a stronger effect on the attainable lateral deflection.

Although Case 2 employed a less restrictive HIC15 limit (A = 100) than Case 3 (A = 50), it produced a lower HIC15 value (7.36 versus 17.24) while achieving a 2.7% greater lateral deflection (1,219.18 versus 1,187.51 mm). Its lateral deflection was the second largest among the six selected designs. To interpret this non-monotonic response, Case 2 produced only 5.1% less lateral deflection than Case 1, whereas Case 1 had an HIC15 value approximately 62.1 times higher (457.02 versus 7.36).

The gross Hybrid III postures of Cases 1 and 2 were broadly similar at 0.10, 0.17, and 0.23 s, as shown in Figure 17. A closer examination, however, showed that Case 1 underwent a secondary head-contact event at approximately 0.17 s. This event coincided with a concentrated x-direction acceleration peak and produced a maximum resultant acceleration of 153.96 g during the critical HIC15 interval from 0.169 to 0.172 s. In Case 2, the critical interval occurred earlier, from 0.090 to 0.105 s, with a substantially lower maximum resultant acceleration of 22.93 g and without a comparable secondary acceleration peak (Figure 18). Because all other analysis conditions were unchanged, the large HIC15 difference is attributed to the different local head-contact responses produced by the two front-end geometries rather than to a clearly distinguishable difference in gross dummy motion.

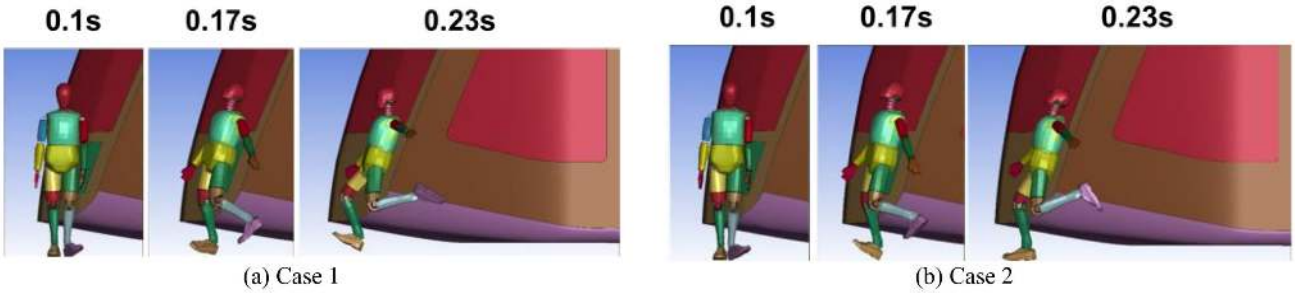


Figure 17 Comparison of Hybrid III kinematics for Cases 1 and 2 at 0.10, 0.17, and 0.23 s.

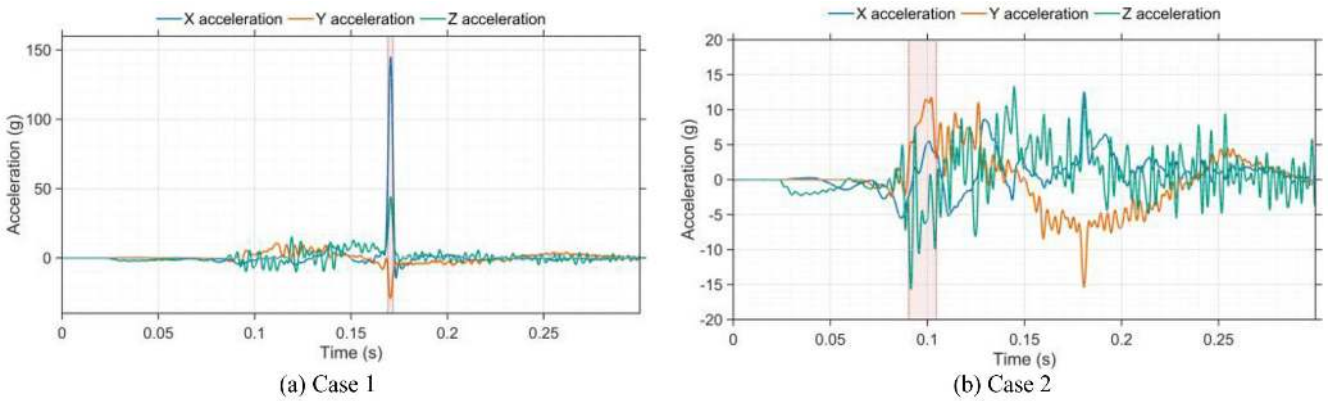


Figure 18 Directional head-acceleration histories for (a) Case 1 and (b) Case 2.

6 DISCUSSION

The baseline results demonstrate why HIC15 and lateral deflection must be considered together. HIC15 was low for both pedestrian representations, whereas lateral deflection failed by a wide margin. A design decision based only on head response would therefore overlook the failure to satisfy the prescribed lateral-deflection criterion. The different head-contact behaviors of Hybrid III and VIVA+ AM50 are also consistent with evidence that HBM and ATD responses should not be regarded as interchangeable (Lackner et al. 2023). Nevertheless, both models identified the same baseline deficiency, namely insufficient lateral deflection, despite their different local kinematics.

The optimization results clarify the respective roles of the HIC15 response constraint and the design-variable side constraints. Increasing α and β generally promotes lateral deflection, but HIC15 does not necessarily vary monotonically because the timing and location of torso, shoulder, and head contact may change with geometry. This behavior is consistent with the competing contact mechanisms reported by Chevalier et al. (2019). The Global Response Surface Method is appropriate for this problem because it combines response-surface-based optimization with global exploration and updates the approximation using each newly obtained high-fidelity response.

Case 2 particularly illustrates this non-monotonic relationship. Although its HIC15 limit (A = 100) was less restrictive than that of Case 3 (A = 50), Case 2 achieved both a lower HIC15 (7.36 versus 17.24) and a greater lateral deflection (1,219.18 versus 1,187.51 mm). Compared with Case 1, Case 2 produced only 5.1% less lateral deflection, whereas the HIC15 of Case 1 was approximately 62.1 times higher. The Case 1 response was governed by a secondary head-contact event at approximately 0.17 s and the associated concentrated x-direction acceleration peak, which was not observed in Case 2. The large difference in HIC15 therefore resulted primarily from local head-contact loading rather than from a clearly distinguishable difference in gross dummy motion.

The designs satisfying HIC15 ≤ A and D ≥ 800 mm during the initial DOE should not be confused with the original baseline geometry, which failed the 800-mm lateral-deflection criterion. These initial designs were already geometrically modified samples within the prescribed design space. Continued GRSM optimization increased the verified lateral-deflection margin within the same constraints and quantified the influence of A and B on the selected designs. This comparison is relevant to practical tram development, in which project-specific requirements, design margins, and manufacturing limitations may need to be considered in addition to the minimum standard criteria.

The proposed framework differs from studies that compare predefined tram fronts by embedding an existing production-oriented finite element mesh in a numerical optimization loop. It is therefore applicable when exterior

styling, packaging, and structural interfaces restrict the redesign space. The method also separates geometric screening from simulation-based acceptance: some selected designs did not satisfy every α or β recommendation but satisfied both Type A collision-response criteria, illustrating the alternative assessment route provided by CEN/TR 17420. The six cases represent parametric design conditions for examining practical trade-offs and should not be interpreted as additional requirements of the standard.

The present study focused on the comparative influence of tram-front geometry within the prescribed CEN/TR 17420 Type A assessment. Material failure and detailed laminated-glass behavior were not represented, although these mechanisms may affect local head-contact response (Jezdik et al. 2023). Future work should therefore investigate more realistic windshield models, quantify the effects of material and geometric uncertainties, and validate the selected design through physical component or full-scale testing.

Among the selected designs, Cases 2 and 3 provided relatively large simulated margins to both collision-response criteria. These margins provide a rational basis for comparing feasible designs but should not be interpreted as a probabilistic robustness assessment. A subsequent study should quantify the effects of material-property and geometric-tolerance uncertainties and compare the numerical responses with physical test results. Accordingly, the practical value of the case comparison lies in quantifying the trade-off among lateral deflection, head-injury response, and the allowable extent of front-end modification.

7 CONCLUSIONS

A standards-oriented shape-optimization workflow was developed to improve the passive safety of an existing tram front. At the 50% offset position, the baseline design satisfied the HIC15 criterion but produced lateral deflections of 582.62 mm for Hybrid III and 321.58 mm for VIVA+ AM50, both below the required 800 mm.

Mesh morphing and GRSM identified one selected design from each of the six optimization cases that satisfied both Type A collision-response criteria. Across the selected designs, lateral deflection ranged from 895.25 to 1,284.46 mm, while HIC15 ranged from 7.36 to 711.49. Within the analyzed cases, the design-variable upper bound B had a more pronounced influence on the attainable lateral deflection than the HIC15 upper limit A. Case 2 achieved the second-largest lateral deflection of 1,219.18 mm with HIC15 = 7.36. Case 1 produced only 5.1% greater lateral deflection than Case 2, but its HIC15 was approximately 62.1 times the Case 2 value because of the concentrated acceleration pulse associated with a secondary head-contact event.

The case comparison demonstrates that satisfying the minimum collision-response criteria is not the only consideration in selecting a practical design. The six cases quantify the trade-off among lateral deflection, HIC15 response, and the allowable extent of front-end modification under alternative design conditions. The proposed workflow therefore provides a practical means of converting the CEN/TR 17420 Type A assessment criteria into quantitative shape-design decisions for new or existing tram fronts. Further development should focus on more realistic windshield modeling, uncertainty analysis, and validation through physical component or full-scale testing.

Acknowledgements

The authors acknowledge the institutional support provided for this study. This was supported by Korea National University of Transportation Industry–Academy Cooperation Foundation in 2024.

Author's Contributions: Conceptualization, J. Lee and H.-L. Jang; methodology, J. Park, M. Cho and H.-L. Jang; software, J. Park and M. Cho; validation, J. Park, M. Cho and J. Lee; formal analysis, J. Park and M. Cho; investigation, J. Park and M. Cho; data curation, J. Park; writing—original draft, J. Park and M. Cho; writing—review and editing, J. Lee and H.-L. Jang; visualization, J. Park; supervision, J. Lee and H.-L. Jang; project administration, H.-L. Jang; funding acquisition, H.-L. Jang. All authors read and approved the final manuscript.

Data Availability statement: The data supporting the findings of this study are available from the corresponding author upon reasonable request.

Editor: Marcilio Alves.

References

Ahn, S.H., Jung, H.S., Kim, J.S., Son, S.W. (2021). Crashworthiness analysis and shape design optimization of thin-walled corrugated tubes under axial impact. Journal of the Korea Academia-Industrial Cooperation Society 22(5):128–135.

Altair Engineering Inc. (2021). Altair HyperStudy training manual. Altair Engineering, Troy, MI.

Asadinia, N., Khalkhali, A., Saranjam, M.J. (2018). Sensitivity analysis and optimization for occupant safety in automotive frontal crash test. Latin American Journal of Solids and Structures 15(7):e55. https://doi.org/10.1590/1679-78254666

Bethell, C.J.D., Sharma, S., Winnett, J., Hughes, D.J. (2024). Pedestrian interaction with a novel urban light rail vehicle: implications for multi-modal crash compatibility standards. Future Transportation 4(4):1177–1204. https://doi.org/10.3390/futuretransp4040057

CEN (2019). CEN/TR 17420: Railway applications—vehicle end design for trams and light rail vehicles with respect to pedestrian safety. European Committee for Standardization, Brussels.

Chevalier, M.-C., Brizard, D., Beillas, P. (2019). Study of the possible relationships between tramway front-end geometry and pedestrian injury risk. Traffic Injury Prevention 20(1):107–113. https://doi.org/10.1080/15389588.2018.1536823

Decker, W., Koya, B., Pak, W., Untaroiu, C.D., Gayzik, F.S. (2019). Evaluation of finite element human body models for use in a standardized protocol for pedestrian safety assessment. Traffic Injury Prevention 20(S2):S32–S36.

Devane, K., Hsu, F.-C., Koya, B., Davis, M., Weaver, A.A., Gayzik, F.S., Guleyupoglu, B. (2023). Assessment of finite element human body and ATD models in estimating injury risk in far-side impacts using field-based injury risk. Accident Analysis & Prevention 192:107262.

Forrester, A.I.J., Sóbester, A., Keane, A.J. (2008). Engineering design via surrogate modelling: a practical guide. Wiley, Chichester.

Forsberg, J., Nilsson, L. (2006). Evaluation of response surface methodologies used in crashworthiness optimization. International Journal of Impact Engineering 32(5):759–777. https://doi.org/10.1016/j.ijimpeng.2005.01.007

Gaca, S., Franek, L. (2021). Pedestrian fatality risk as a function of tram impact speed. Open Engineering 11(1):1105–1113. https://doi.org/10.1515/eng-2021-0110

Jezdik, R., Sebik, M., Kubovy, P., Marsik, F., Lopot, F., Hajkova, B., Hylmarova, D., Havlicek, M., Stocek, O., Doubek, M., Tikkanen, T., Svoboda, M., Jelen, K. (2023). Pedestrian safety in frontal tram collision, Part 2: laminated glass as a crucial part of the absorption and deformation zone—its impact test and analysis. Sensors 23(21):8974. https://doi.org/10.3390/s23218974

Ji, Y.H., Lim, S.H., Park, Y.I. (2021). Collision test for the collision simulation of the urban railway vehicle connector absorber. Transactions of the Korean Society of Automotive Engineers 29(8):733–740.

John, J., Klug, C., Kranjec, M., Svenning, E., Iraeus, J. (2022). Hello, world! VIVA+: a human body model lineup to evaluate sex-differences in crash protection. Frontiers in Bioengineering and Biotechnology 10:918904. https://doi.org/10.3389/fbioe.2022.918904

Kim, J.S., Jung, H.S. (2021). Experimental crashworthiness evaluation of tubular energy absorber with circular cutting mechanism. Journal of the Korean Society for Railway 24(2):188–193.

Lackner, C., Heinzl, P., Leo, C., Klug, C. (2023). Investigations on tram–pedestrian impacts by application of virtual testing with human body models. European Transport Research Review 15:22. https://doi.org/10.1186/s12544-023-00595-0

Lackner, C., Heinzl, P., Rizzi, M.C., Leo, C., Schachner, M., Pokorny, P., Klager, P., Buetzer, D., Elvik, R., Linder, A., Klug, C. (2022). Tram to pedestrian collisions—priorities and potentials. Frontiers in Future Transportation 3:913887. https://doi.org/10.3389/ffutr.2022.913887

Lopot, F., Tomsovsky, L., Marsik, F., Masek, J., Kubovy, P., Jezdik, R., Sorfova, M., Hajkova, B., Hylmarova, D., Havlicek, M., Stocek, O., Doubek, M., Tikkanen, T., Svoboda, M., Jelen, K. (2023). Pedestrian safety in frontal tram collision, Part 1: historical overview and experimental-data-based biomechanical study of head clashing in frontal and side impacts. Sensors 23(21):8819. https://doi.org/10.3390/s23218819

Naznin, F., Currie, G., Logan, D. (2016). Exploring the impacts of factors contributing to tram-involved serious injury crashes on Melbourne tram routes. Accident Analysis & Prevention 94:238–244. https://doi.org/10.1016/j.aap.2016.06.008

Pajot, J. (2013). Optimal design exploration using global response surface method: rail crush. Altair Engineering, Troy, MI.

Peng, Y., Chen, F., Yu, S., Wang, B., Xiao, J. (2024). Assessment of pedestrians' head and lower limb injuries in tram–pedestrian collisions. Biomimetics 9(1):17. https://doi.org/10.3390/biomimetics9010017

Spirk, S., Spicka, J., Vychytil, J. (2022). Numerical simulation of tram collision with pedestrian. MATEC Web of Conferences 357:02011.

Tomsovsky, L., Lopot, F., Kubovy, P., Jezdik, R., Hajkova, B., Rulc, V., Jelen, K. (2022). Tram–pedestrian collisions: the severity of head injuries due to secondary impact with the surrounding infrastructure (ground). 2022 International Conference on Electrical, Computer, Communications and Mechatronics Engineering, pp. 1–6. https://doi.org/10.1109/ICECCME55909.2022.9988616

Usta, F., Türkmen, H.S., Scarpa, F. (2018). Crashworthiness optimization of nested and concentric circular tubes using response surface methodology and genetic algorithm. Latin American Journal of Solids and Structures 15(5):e42.

Wang, G.G., Shan, S. (2007). Review of metamodeling techniques in support of engineering design optimization. Journal of Mechanical Design 129(4):370–380. https://doi.org/10.1115/1.2429697

Wdowicz, D., Ptak, M. (2023). Numerical approaches to pedestrian impact simulation with human body models: a review. Archives of Computational Methods in Engineering 30:4687–4709. https://doi.org/10.1007/s11831-023-09949-2

Weber, T., Muser, M., Schmitt, K.-U. (2015). Optimising the design of tramways to mitigate injury risk in pedestrian impacts. Proceedings of the 2015 IRCOBI Conference, Lyon, pp. 339–349.

Yay, İ., Demirci, E., Özcan, A.R. (2025). Multi-objective optimization of aluminum foam-filled battery boxes for electric vehicle safety. Latin American Journal of Solids and Structures 22(3):e8408. https://doi.org/10.1590/1679-7825/e8408